scientific reports

Check for updates

OPEN

Transforming waste into value: Single-step in situ synthesis of magnetic porous carbon composite adsorbents from sugarcane bagasse and iron scrap

Sirinad Mahawong[1,8], Parichart Onsri[2,8], Piyatida Thaveemas[2], Sulawan Kaowphong[3], Supinya Nijpanich[4], Natthanan Rattanachueskul[1], Supanna Techasakul[2], Laemthong Chuenchom[1,5]✉ & Decha Dechtrirat[2,6,7]✉

The demand for sustainability is driving research into new ways to make use of waste products. Porous adsorbents with magnetic properties are reusable and do not require a significant external energy source. They are well-suited to the task of decontaminating water on a large scale and, if benignly synthesized from waste products, they would meet the demand for sustainability. In this research, an in situ single-step synthesis is developed that generates a magnetic porous carbon composite from iron scrap and sugarcane bagasse, both of which are abundant waste products. This procedure combines the processes of carbonization, magnetization, and activation in one step. Iron scrap serves as both a magnetic precursor and a self-activating agent, so no additional chemical activators are required. The large surface area (505 m^2/g) of the synthesized magnetic porous carbon composite adsorbent and its large capacity for tetracycline adsorption (687.6 mg/g) are suitable properties for the treatment of contaminated wastewater. The synthesis process is straightforward, and the use of waste materials to fabricate an adsorbent that retains its performance even after five cycles of adsorption and desorption ensures both cost-effectiveness and sustainability to support the concept of the circular economy.

Keywords Waste valorization, Iron scrap, Circular economy, Sugarcane Bagasse, Reusable adsorbent

As industrial and agricultural activity intensifies worldwide, the problem of water pollution is one of increasing concern[1]. Among the most problematic water contaminants, pharmaceutical residues of antibiotics present a particularly serious threat to human health[2]. Since the antibiotic tetracycline (TC) is administered to livestock as well as humans, it can enter the water supply through agricultural runoff and wastewater from the pharmaceutical sector[3]. In wastewater, TC cannot easily be broken down and has a tendency to accumulate within surface and groundwater, and sometimes in sources of drinking water. Over time, it can destroy the aquatic environment, killing useful microorganisms and promoting antimicrobial resistance. Given that human health can also be adversely affected by the presence of TC in water sources, it is essential that a sustainable approach be found for the safe and efficient removal of TC from wastewater[4].

Common approaches to eliminate contaminants include biodegradation[5]and oxidation[6,] but adsorption[7]is perhaps the cheapest, easiest, and most efficient method, and has the advantage of not producing dangerous byproducts. Adsorption involves the adherence of target pollutants to a solid adsorbent surface. To work effectively, the adsorbent requires good porosity, a large surface area, and suitable functional groups[8]. Materials

[1]Division of Physical Science, Faculty of Science, Prince of Songkla University, Songkhla 90112, Thailand. [2]Laboratory of Organic Synthesis, Chulabhorn Research Institute, Bangkok 10210, Thailand. [3]Department of Chemistry, Center of Excellence in Materials Science and Technology, Faculty of Science, Chiang Mai University, Chiang Mai 50200, Thailand. [4]Synchrotron Light Research Institute, Nakhon Ratchasima 30000, Thailand. [5]Center of Excellence for Innovation in Chemistry, Faculty of Science, Prince of Songkla University, Songkhla 90112, Thailand. [6]Department of Materials Science, Faculty of Science, Kasetsart University, Bangkok 10900, Thailand. [7]Specialized Center of Rubber and Polymer Materials for Agriculture and Industry (RPM), Faculty of Science, Kasetsart University, Bangkok 10900, Thailand. [8]These authors contributed equally: Sirinad Mahawong and Parichart Onsri. ✉email: laemthong.c@psu.ac.th; fscidcd@ku.ac.th

based on carbon, such as biochar, activated carbon, carbon nanotubes, and graphene oxide, offer all of these qualities, while their stability enables long-term use[9].

The use of waste biomass to produce carbon materials offers a valuable means of eliminating the environmental challenges the waste poses[10]. Sugarcane bagasse (BG) is an important agricultural byproduct that must be managed effectively to avoid environmental harm[11], so its conversion into products for use in agriculture, energy, or industry offers a means to eliminate large volumes of potentially damaging waste. The suitability of BG as a carbon source stems from the high levels of cellulose, hemicellulose, and lignin it contains[12]. The carbonization of BG allows the sustainable production of carbon-based adsorbents that can decontaminate wastewater, while adding value to an agricultural waste, supporting environmental protection, and promoting the circular economy.

Carbon adsorbents are usually powders, which are difficult to recover after use. The increased energy and time required to recover them raise operating costs[13], discouraging the adoption of carbon adsorbents in large-scale water treatment systems. However, the introduction of magnetic properties to carbon-based materials can address these issues by making separation cheap and simple with an external magnetic field. Such processes are inexpensive and can be scaled up easily[14]. Magnetic carbon composite adsorbents can efficiently remove pollutants and are easy to recover for reuse. Their reusability extends their lifespan, reducing waste generation and overall treatment costs. Furthermore, the management of adsorbent movement and retrieval through magnetic fields allows for greater operational efficiency and flexibility in system design[15].

The production of magnetic carbon composite adsorbents typically involves three main stages: carbonization, activation, and magnetization. The carbonization step involves the heating of organic material in the absence of oxygen, forming a material rich in carbon, whose surface area and porosity can be enhanced by chemical or physical activation. Meanwhile, the magnetization process results in a carbon composite material with magnetic properties that enhance separability. These three steps are often performed sequentially, but this approach can be time-consuming, energy-intensive, and costly, limiting scalability for large-scale applications[16]. Therefore, combining the steps represents an interesting alternative. It is possible to combine carbonization and activation, followed by a separate magnetization step[17,18]. Alternatively, carbonization and magnetization can be combined, while activation takes place separately[19]. However, integrating all three steps delivers greater efficiency[20,21]. The single-step process saves time, energy, and cost, and is more attractive for large-scale applications.

The porosity and surface area of a carbon material can be increased through the use of activating agents. Among the most widely used activating agents are phosphoric acid (H_3PO_4), zinc chloride ($ZnCl_2$) and potassium hydroxide (KOH)[22,23]. These compounds, however, carry an associated cost in both financial and environmental terms. Alternatively, iron may be used since it can activate pores and provide magnetic properties[24]. This approach simplifies the synthesis process, reduces reliance on more costly agents, and improves the performance of the adsorbent. More recently, a single-step process, which combined carbonization, activation, and magnetization while using iron salts for magnetism and activation, was shown to be an efficient and cost-effective method[25].

Traditionally, magnetic adsorbents are synthesized using commercial iron salts such as $FeCl_2$, $FeCl_3$, $FeSO_4$, and $Fe(NO_3)_3$[24,26,] but these materials are all expensive compared with iron scrap, which is a steel industry byproduct rich in a range of iron oxides[27]. The use of iron scrap to produce magnetic adsorbents would not only support the development of low-cost, high-performance materials for water purification, but also help reduce the environmental challenge posed by the accumulation of iron scrap. This approach would align with the principles of the circular economy, turning industrial waste into valuable resources while advancing sustainable environmental remediation technologies.

In this study, a unified approach is proposed which combines the three steps of carbonization, activation, and magnetization in one process, in which iron scrap acts as a pore activator and a source of magnetism. The use of a single-step in situ synthesis is simpler, faster, and cheaper than conventional approaches, and requires less energy. A similar technique cannot be found in the literature, and therefore, this is a significant contribution to the field of magnetic carbon composite adsorbent synthesis. The production of high-performance, reusable adsorbents from waste materials will increase the sustainability of cost-effective water treatment and showcase the role of waste-derived materials in promoting the principles of the circular economy.

Materials and methods

Materials

This study used sugarcane bagasse (BG) (40–50% cellulose, 25–35% hemicellulose, 15–25% lignin, and other minor minerals) as a source of carbon. BG was supplied by the Eastern Sugar and Cane Public Company Limited in Sa Kaeo, Thailand. The magnetic precursor was iron scrap obtained from Songkhla, in southern Thailand. HCl (37%) was supplied by J.T. Baker and Merck, and TC was from TCI Chemicals. The experiments used deionized (DI) water, and all chemicals were of analytical reagent grade.

Preparation of magnetic porous carbon composite

Iron scrap solution preparation: Initially, the iron scrap was cleaned of dust, and then finely pulverized using a 500 g multifunction disintegrator. The iron scrap powder was then dissolved in concentrated HCl in the ratio of 0.04 g/mL. The solution was filtered and diluted using DI water in a ratio of 1:3 to obtain an acidic iron solution, which contained around 2 g/L of iron ions. The measurement was obtained via inductively coupled plasma optical emission spectrometry (ICP-OES, Avio500, PerkinElmer). This solution was then placed in storage until required for the synthesis of the magnetic carbon composite adsorbent.

Sugarcane bagasse waste preparation: The bagasse was collected following three cycles of juice extraction, washed in DI water to ensure the removal of impurities, sugar, and residual dirt, and dried thoroughly for 48 h at 90 °C. The dried bagasse was chopped, ground, and sieved through a vibrating screen to ensure a particle size of 710 µm. The resulting material was labeled BG and placed in a desiccator for storage.

Magnetic porous carbon composite preparation: Magnetic porous carbon composite (MPC) was prepared by adding 50 mL of the 2 g/L iron stock solution to 2.5 g of BG. The mixture was stirred at 150 rpm for 15 h at room temperature, then allowed to dry overnight at 90 °C. The dried product was then heated in a furnace at 2 °C/min to 800 °C and held at that temperature for 2 h. Following pyrolysis, the sample was washed repeatedly in hot water until the pH value of the runoff water became neutral. The sample was dried, and the final product was labeled MPC-Fe2. The same process was followed to prepare MPC with an iron concentration of 1 g/L (MPC-Fe1), and a control porous carbon (PC) sample was produced without iron, using the same acid concentration.

Materials characterization

The phase composition and crystallinity of materials were identified by X-ray diffraction (XRD, Philips X'Pert MPD). Vibrating sample magnetometry (VSM, Lakeshore) was used to measure the magnetic properties at 298 K. Nitrogen adsorption-desorption analysis (Micromeritics 3 Flex analyzer) was carried out at 77 K, while surface area and porosity were assessed using the Brunauer-Emmett-Teller (BET) method. The morphology, surface texture, and distribution of iron particles were studied with scanning electron microscopy coupled with energy dispersive X-ray spectroscopy (SEM, Quanta450 and EDX, X-Max 80, Oxford). Iron particles in the carbonaceous structure were then examined using transmission electron microscopy (TEM, JEOL JEM-2010 and JEM-2100 Plus). Elemental distribution mappings were produced by scanning TEM–EDS. Fourier transform infrared spectroscopy in attenuated total reflection mode (ATR–FTIR, VERTEX 70, Bruker) was used to identify the functional groups of materials. The elemental composition of surfaces and sample oxidation states were investigated by X-ray photoelectron spectroscopy (XPS) (PHI5000 VersaProbe II, ULVAC-PHI) performed at the SUT-NANOTEC-SLRI Joint Research Facility, Synchrotron Light Research Institute (SLRI), Thailand. UV-Vis spectroscopy (UV 2600, Shimadzu) was performed to establish TC concentrations during adsorption studies. Iron concentration was determined using inductively coupled plasma (ICP) analysis (ICP-OES, Avio500, PerkinElmer).

Adsorption study

Adsorption kinetics: Kinetics experiments were carried out to elucidate the rate at which TC is removed from solution by the magnetic carbon composite adsorbent. Briefly, 0.010 g of adsorbent was added to 100 mL of a 100 mg/L TC solution and maintained under constant shaking at 25 ± 1 °C. The adsorption study was conducted in triplicate to ensure the reliability of the data. At predetermined time intervals (15, 30, 45, 60, 90, 180, 240, 300, 360, 480, 600, 720, 1440, 1800, 2160, and 2880 min), aliquots were withdrawn, and the adsorbent was rapidly separated using an external magnet. The TC concentration in the supernatant was measured by UV-Vis spectrophotometry at λ = 357 nm. The amount of TC adsorbed at time t, q_t (mg/g), was calculated from Eq. (1):

$$q_t = \frac{(C_0 - C_t)V}{m} \tag{1}$$

where C_0 and C_t are the initial and time-t concentrations of TC (mg/L), V is the solution volume (L), and m is the mass of adsorbent (g). The experimental data were fitted using the non-linear pseudo-first-order (PFO) and pseudo-second-order (PSO) kinetic models, as presented in the equations in Note S1 (Supplementary Information).

Adsorption isotherms: Adsorption isotherms were used to evaluate and predict the capacities of materials in terms of TC adsorption. An adsorbent dose of 0.010 g was added to 100 mL of TC solutions with initial concentrations of 25, 75, 100, 150, 300, 500, 750, 1000, 1250, and 1500 mg/L. The adsorption study was conducted in triplicate to ensure the reliability of the data. After shaking the mixture for 48 h at a temperature of 25 ± 1 °C, the magnetic carbon composite adsorbent was separated with an external magnet. The absorbance of the supernatant was determined by UV-Visible spectrophotometry at λ = 357 nm. The amount of TC adsorbed was calculated from Eq. (2)

$$q_e = \frac{(C_0 - C_e)V}{m} \tag{2}$$

in which C_e indicates the equilibrium concentration of the TC solution (mg/L), V denotes the volume of the solution (L), and m represents the adsorbent mass (g). The experimental data were fitted using various non-linear models, including the Langmuir, Freundlich, Temkin, and Guggenheim-Anderson-de Boer (GAB) models, as presented in the equations in Note S1, to describe the adsorption behavior and identify the best-fitting model for the observed data.

Adsorbent reusability

To desorb TC, the adsorbent was placed in a 120 mL bottle which contained 20 mL of 75% EtOH solution. The bottle was shaken for 24 h at 25 ± 1 °C to allow desorption to take place. The adsorbent was then repeatedly washed in DI water, and dried for 1 h at 110 °C. It was then used again. In all, five adsorption-regeneration cycles were carried out to assess the reusability of the material. Iron leaching after each adsorption cycle was determined using inductively coupled plasma (ICP) analysis. The entire adsorption study, including the desorption, regeneration cycles, and iron leaching measurements, was conducted in triplicate to ensure the reliability and reproducibility of the results.

Results and discussion

Materials characterization

In industrial surroundings, moisture and oxygen cause iron scrap to rust more readily, leading to a phase transformation from metallic iron to iron oxide, which leads to the formation of structural defects, increasing porosity and causing the material to weaken[28,29]. These oxidized phases are excellent, cheap iron precursors. According to the XRF analysis, the iron scrap used in this work contained iron oxides (81.95%) (Table S1) while the XRD analysis (Fig. 1a) showed that Fe_2O_3(No. 00–039–1346)[30]was present along with various oxyhydroxides including α-FeOOH (No. 00–029–0713) and γ-FeOOH (No. 00–044–1415)[31].

When the iron scrap was dissolved in concentrated HCl, the acid converted the iron oxide into soluble iron ions, as follows[32–34]:

$$Fe_2O_3 + Fe + 6HCl \rightarrow 3\ FeCl_2 + 3H_2O \quad (3)$$

$$Fe_2O_3 + 6HCl \rightarrow 2\ FeCl_3 + 3H_2O \quad (4)$$

$$FeOOH + 3HCl \rightarrow FeCl^{2+} + 2Cl^{-} + 2H_2O \quad (5)$$

When BG was immersed in the iron solution, Fe^{2+} and Fe^{3+}were adsorbed on outer surfaces and within the pore network. The ions formed bonds with the electron-rich oxygen atoms in the hydroxyl and ether groups of cellulose[35], anchoring the iron in the BG matrix, where it was transformed during the carbonization stage.

Figure 1a presents XRD patterns which show the structural differences between iron scrap, MPC-Fe2-raw, MPC-Fe1, and MPC-Fe2. The results imply that structural changes occurred during synthesis. Following pyrolysis at 800 °C, MPC-Fe1 and MPC-Fe2 samples exhibited sharper diffraction peaks than MPC-Fe2-raw, suggesting greater crystallinity as a result of the high-temperature treatment. Iron phases of Fe_3O_4 and Fe^0 (metallic iron) were detected. The characteristic peaks of Fe_3O_4 at 30.13°, 35.48°, 43.12°, 53.50°, 57.00°, and 62.63° 2θ correspond to the (220), (311), (400), (422), (511), and (440) crystallographic planes. Fe^0 was identified from the peaks at 44.6° and 82.35° 2θ, which align with the (110) and (211) planes. The observed phases all matched the standard JCPDF references for Fe_3O_4(No. 01–075-0033)[36] and Fe^0(No. 00–001–1262)[37].

The magnetic phases in the MPC materials formed as a consequence of redox reactions and carbothermal reduction during pyrolysis, as explained in earlier works[38]. The larger iron precursor content generated a greater proportion of magnetic phases during synthesis. Evidence for this is seen in the threefold intensity of the Fe_3O_4 peak of MPC-Fe2 at (311) compared with MPC-Fe1. The higher Fe_3O_4 peak intensity in the pattern of MPC-Fe2 indicate that greater levels of iron precursor content promoted more oxidation, causing more Fe_3O_4 to form[39]. However, both samples showed similar intensity levels for the Fe^0 peaks, suggesting that reduction to Fe^0 was primarily affected by the carbon precursor rather than the iron precursor, from which it was inferred that reduction occurred in a similar manner in both samples.

The XRD patterns of the carbonized samples indicated that turbostratic carbon was present in the samples. This particular structure has randomly disordered graphene layers that result in the presence of both ordered and disordered regions. The patterns show LDCC (less-developed crystalline carbon) and MDCC (more-developed crystalline carbon), with LDCC confirmed by the wide hump at around 20–30° 2θ, suggesting lower crystallinity and greater disorder in the structure[40]. The hump corresponds to the disordered turbostratic regions, which feature misaligned graphene layers. Meanwhile, the slight peak at 26° 2θ corresponds to the MDCC region, indicative of more ordered crystalline carbon, which may be a graphitic or similarly organized carbon form. In the pattern of MPC-Fe2, the more pronounced MDCC peak, slightly stronger than the broad LDCC hump, suggested a crystalline structure comprising ordered carbon regions as part of a turbostratic structure. However, such obvious separation between the peak of MDCC and the hump of LDCC was not present in the pattern of MPC-Fe1, as the MDCC peak overlapped the wide hump. Although the right shoulder of the hump was raised

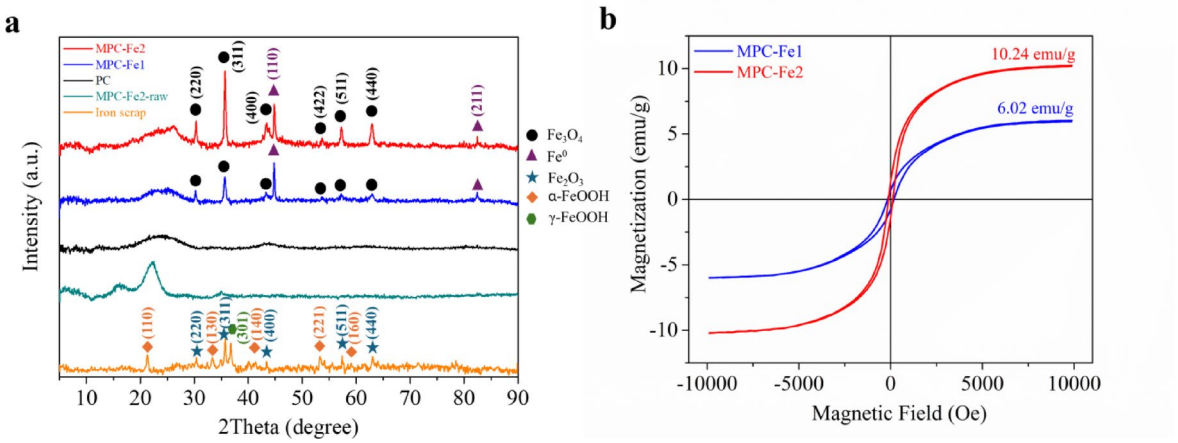

Fig. 1. (**a**) XRD patterns of all prepared samples and (**b**) VSM analysis of the synthesized magnetic porous carbon composite materials.

somewhat, indicating the presence of at least some ordered crystalline regions, albeit fewer than for MPC-Fe2. This difference indicated a less-developed carbon structure by comparison with MPC-Fe2, which benefitted from the catalytic effect of the higher iron content. The synergistic combination of turbostratic carbon and magnetic phases of Fe_3O_4 and Fe^0[41] contributes to the adsorption and magnetic properties, which give the material its dual functionality.

Figure 1b presents the VSM analysis, showing the magnetic properties of MPC-Fe1 and MPC-Fe2. Their ferromagnetic qualities were confirmed by the hysteresis loop[42], while MPC-Fe2 exhibited a greater saturation magnetization (Ms) of 10.24 emu/g, suggesting a higher degree of magnetic responsiveness. The higher saturation magnetization of MPC-Fe2 was due to the greater Fe_3O_4 content, as determined by XRD analysis. Strong magnetic qualities could allow the adsorbent to be quickly and easily recovered and reused following treatment, so lengthy filtration steps would not be necessary.

The pore characteristics of the synthesized porous carbon materials were evaluated using N_2 sorption measurements to determine surface areas, total pore volumes (V_{total} at $p/p^0 = 0.97$) and pore size distributions. All samples exhibited a sharp increase in N_2 adsorption when the pressure was relatively low ($p/p^0 < 0.1$) (Fig. 2a), suggesting strong adsorption interactions in small pores and indicating that the structure was mainly microporous[43]. Mesopores are also present according to the presence of a small hysteresis loop. Mesopores promote better gas diffusion and adsorption[44].

Table 1 compares the porosity parameters, revealing that specific surface area (S_{BET}) and overall porosity increased upon the incorporation of iron into the carbon material. As the iron content increased, pore development was enhanced, leading to a greater total pore volume which in this case was shown as an increase from 0.17 cm^3/g to 0.21 cm^3/g. To further analyze the pore structure, the *t*-plot method was employed to calculate the micropore volume (V_{micro}), from which the mesopore volume (V_{meso}) was subsequently derived. The results indicate an increase in V_{meso} with the addition of iron scrap. Moreover, the Barrett-Joyner-Halenda (BJH) method revealed that the pore size distributions of MPC-Fe1 and MPC-Fe2 were wider than that of PC. The BJH curves (Fig. 2b–d) showed a shift toward larger pore diameters. In addition to rearranging the structure of the pristine carbon (PC), the introduction of iron promoted pore expansion and contributed to the formation of more mesopores[45].

The activation mechanism of PC, MPC-Fe1, and MPC-Fe2 highlighted the role of HCl treatment and iron incorporation in modifying pore structure. For PC, HCl was the sole contributor to activation. HCl partially

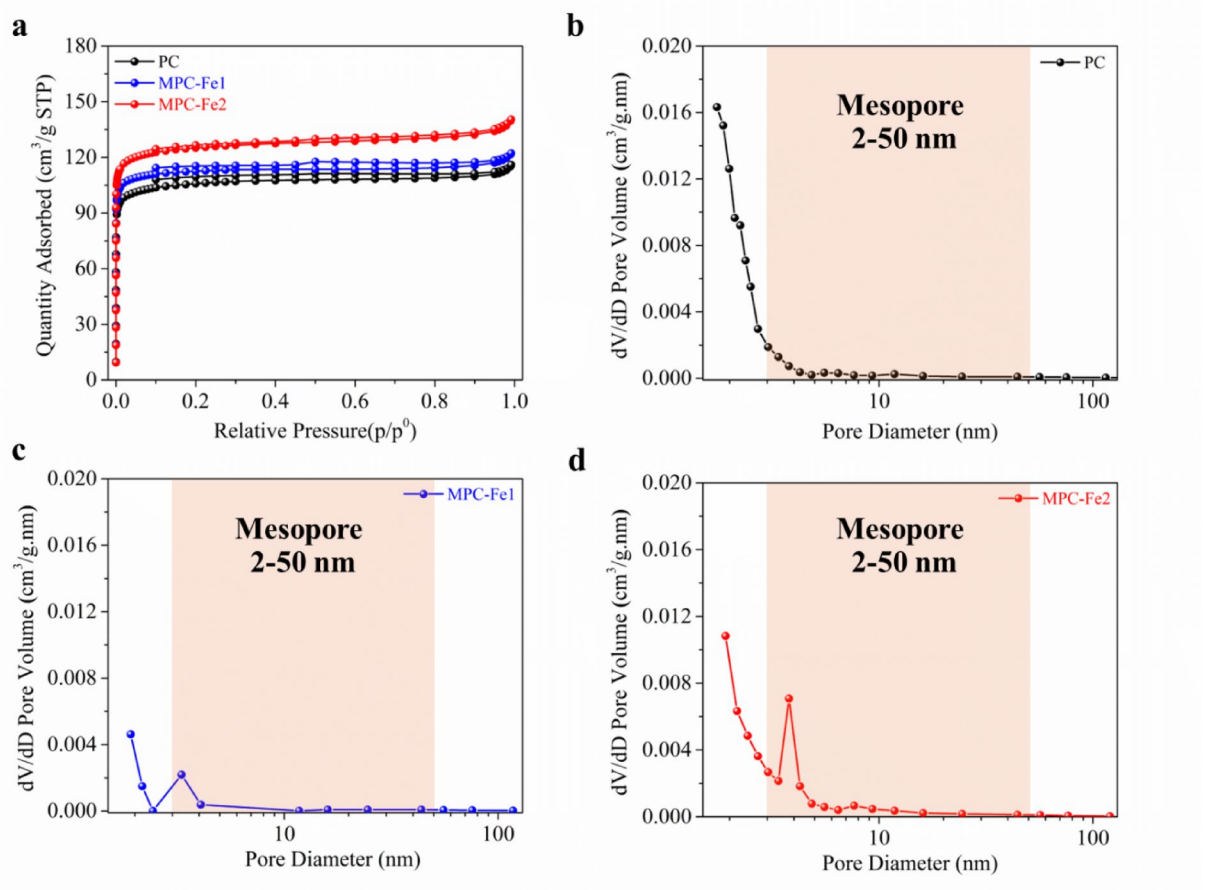

Fig. 2. (**a**) N_2 adsorption-desorption isotherms of all samples. The corresponding pore size distributions, calculated using the BJH method, are shown for (**b**) PC, (**c**) MPC-Fe1, and (**d**) MPC-Fe2.

Samples	S_{BET} (m^2/g)	V_{total} (cm^3/g)	V_{micro} (cm^3/g)	V_{meso} (cm^3/g)	% V_{meso}	Adsorption capacity (mg/g)
PC	425	0.17	0.15	0.02	11.23	179.1 ± 0.3
MPC-Fe1	459	0.18	0.15	0.03	16.60	206.9 ± 0.4
MPC-Fe2	505	0.21	0.17	0.05	21.55	295.2 ± 0.2

Table 1. Pore properties of as-prepared samples and their tetracycline adsorption capacity.

hydrolyzed lignocellulosic biomass components[46], weakening chemical bonds to create a network of micropores (< 2 nm) following pyrolysis[47,48]. HCl also promoted oxidation, which in turn removing unstable organic matter and affecting the pore structure by producing functional groups that contained oxygen[49,50]. In the case of MPC-Fe1 and MPC-Fe2, the addition of iron scrap to HCl catalyzed the development of both mesopores and micropores[39,51]. Pore expansion was boosted by both iron concentrations used. Structural reorganization was catalyzed by iron during pyrolysis, so the pore network became more open and better integrated, while the pore volume and surface area were increased[52]. In particular, MPC-Fe2 exhibited a moderate increase in mesopore formation (2–50 nm), indicating that the higher iron content promoted mesoporosity and overall porosity. The formation of pores was facilitated by the use of acid and the incorporation of iron, with HCl activation inducing microporosity while iron scrap catalyzed the generation of mesopores. This progressive enhancement from PC to MPC-Fe2 demonstrates the synergy of chemical activation and the catalytic effect of iron in creating high-performance porous carbon materials. In addition to the activation of pore generation, the use of iron scrap also promotes the development of magnetic phases, as explained earlier, allowing the production of materials that can be recovered with a magnetic field.

The FTIR spectra of PC, MPC-Fe1, and MPC-Fe2 (Fig.S1) revealed the presence of diverse functional groups in all the studied materials. The C=O stretching vibration of carbonyl groups was detected at around 1750 cm^{-1}, which could represent quinones or conjugated carboxylic acids[53]. The peaks at approximately 1480 cm^{-1} and 1110 cm^{-1} indicate C–O stretching vibrations which were attributed to phenol, carboxylate, or ether functionalities[54]. The peak at around 2348 cm^{-1} was due to CO_2stretching vibrations from the surrounding atmosphere, an artifact commonly observed in FTIR spectra[55]. Furthermore, the broad O–H stretching band from 2500 cm^{-1} to 3300 cm^{-1} corresponds to carboxylic acid (-COOH) groups[56]. The band at about 3600 cm^{-1} was attributed to O–H stretching in phenols or alcohols[57]. The strong peak at 1594 cm^{-1} was designated as C=C stretching in graphitic structures[58], providing evidence of the turbostratic carbon framework in line with the XRD findings. Moreover, the strong absorption band around 550–600 cm^{-1} was a consequence of Fe–O vibrational modes, and demonstrated the incorporation of iron oxide nanoparticles (Fe_3O_4) in the carbon matrix[59]. This band was not produced by non-magnetic samples, thus confirming that iron oxide was integrated within the magnetic porous carbon composite structure.

The preliminary adsorption results under the following conditions—adsorbent: 0.010 g, initial tetracycline concentration: 500 mg/L, solution volume: 100 mL, and equilibrium time: 48 h—suggested a varied uptake of TC for the different synthesized porous carbon materials, which was dependent on pore characteristics. MPC-Fe2 offered the greatest surface area and mesopore volume, and duly exhibited the greatest TC adsorption, at 295.2 mg/g. Consequently, MPC-Fe2 was selected for further characterization and a detailed investigation of its adsorption behavior to elucidate the adsorption mechanism and assess its practical applicability.

The SEM-EDS analysis of MPC-Fe2 (Fig. 3) revealed the morphological characteristics and elemental composition of the material. The morphology of the magnetic carbon composite was irregular and porous, and the surface was rough and fragmented. EDS mapping showed that the elements of carbon, oxygen and iron were evenly distributed throughout the material. The carbon signal confirmed that the composite was carbonaceous, and the oxygen signal was derived from surface functional groups, which potentially supported adsorption. EDS mapping also indicated the dense localization of iron and oxygen in certain areas where magnetic particles were embedded. These particles were visible throughout the surface, in varying sizes and shapes. The EDS spectrum presented three clear peaks, associated with the iron Kα (6.4 keV), Kβ (7.1 keV), and Lα (0.7 keV) lines. These results showed that iron was effectively incorporated within the composite material and provided validation of the presence of an iron phase.

The TEM image of MPC-Fe2 in Fig. 4a revealed iron-based nanoparticles within and on the carbon matrix that could enhance the magnetic qualities of the composite. Figure 4b revealed MPC-Fe2 at greater magnification. Graphitic-like turbostratic carbon was observed with a d-spacing of 0.36 nm, corresponding to the (002) plane of graphitic carbon[60]. The turbostratic structure was formed as a consequence of misaligned graphene layers, producing defects and stacking faults, which increased the surface area and availability of active sites, leading to improved adsorption[61,62]. The observed interlayer spacing was consistent with the XRD results, further confirming the structural characteristics of the material. The SAED pattern (Fig. 4c) confirmed crystallinity by the presence of bright spots and diffraction rings that were attributed to Fe_3O_4 and metallic Fe. The composition of MPC-Fe2 shown in Fig. 4d aligned with the SEM-EDS mapping. It can be seen that iron was distributed from both Fe_3O_4 and Fe^0, while oxygen was distributed from Fe_3O_4 and surface functional groups which contained oxygen. Carbon was distributed throughout the porous carbon matrix. It was thus concluded that the iron-based nanoparticles were incorporated throughout the carbon framework.

The surface chemical composition of MPC-Fe2 and the oxidation states of the carbon and iron species were examined through XPS analysis. The survey spectrum (Fig. 5a) shows that iron, oxygen, and carbon were all present. The C 1s spectrum (Fig. 5b) presented peaks associated with C–C/C=C (284.50 eV), C–O–C/C–OH

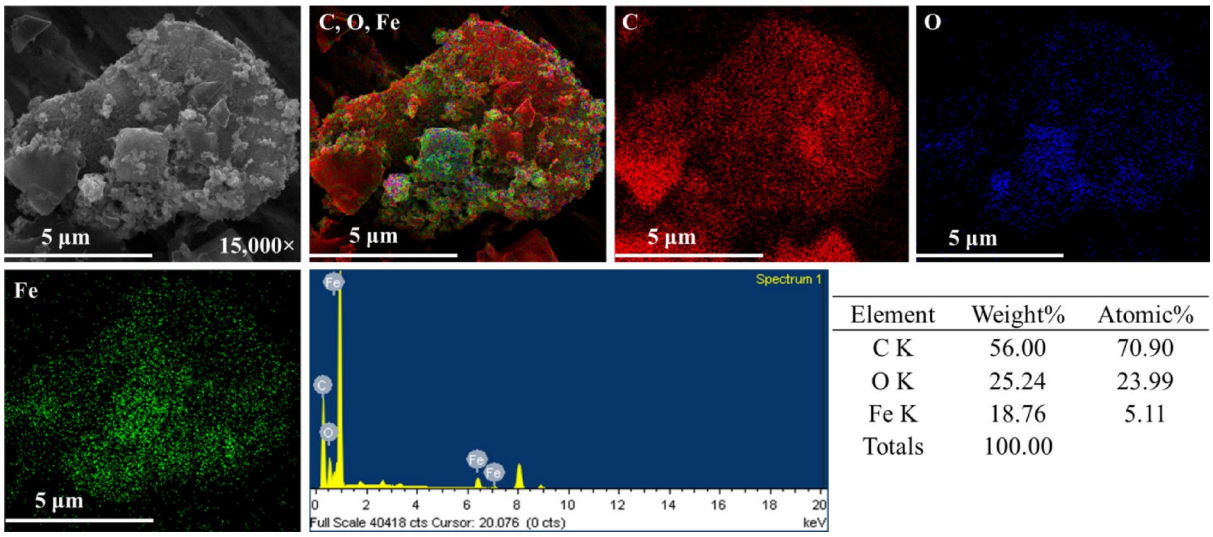

Element	Weight%	Atomic%
C K	56.00	70.90
O K	25.24	23.99
Fe K	18.76	5.11
Totals	100.00	

Fig. 3. SEM-EDS analysis of MPC-Fe2, showing the color-coded distribution of C, O, and Fe elements, along with their respective atomic percentages.

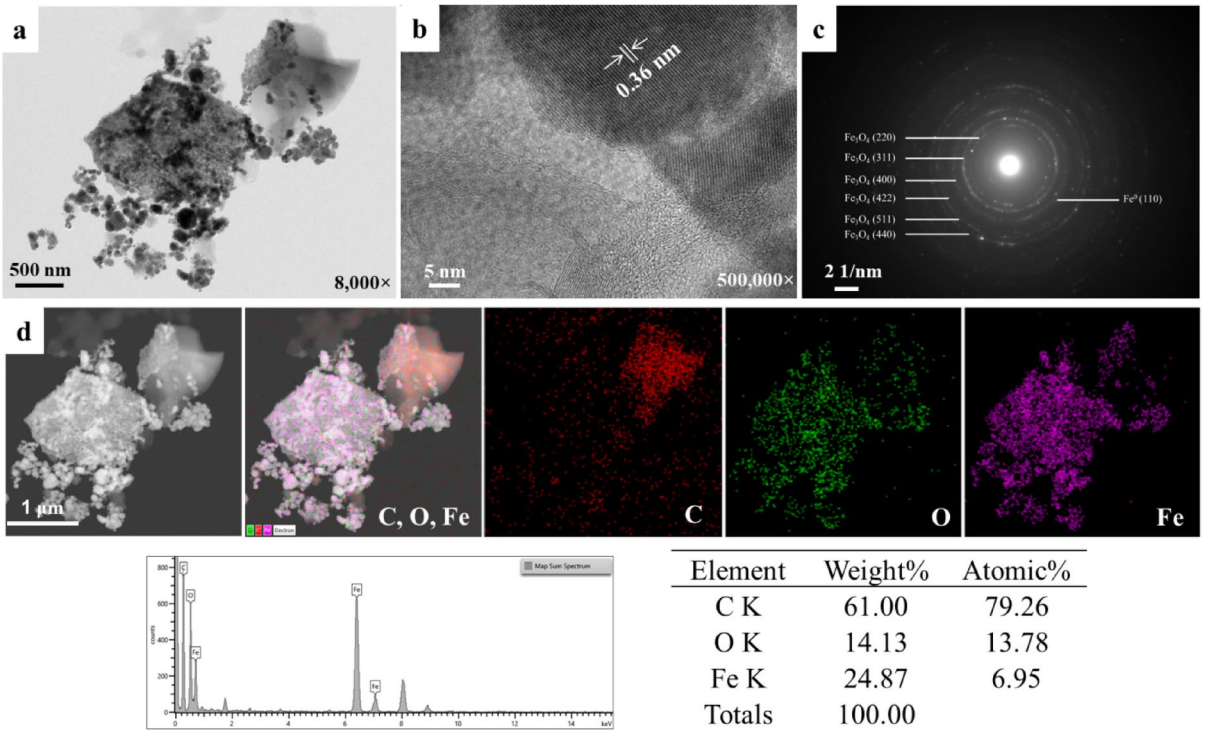

Element	Weight%	Atomic%
C K	61.00	79.26
O K	14.13	13.78
Fe K	24.87	6.95
Totals	100.00	

Fig. 4. (**a**) TEM image of MPC-Fe2 at ×8,000 magnification, (**b**) TEM image at ×500,000 magnification, (**c**) Selected Area Electron Diffraction (SAED), and (**d**) energy-dispersive X-ray spectroscopy (EDS) mapping.

(286.02 eV), C=O (287.60 eV), and COOH (288.74 eV), confirming that carbonization had occurred and oxygenated functional groups had been successfully incorporated during pyrolysis[63,64]. Table S2 shows the existence of a dominant C=C peak in addition to π–π* resonance (290.56 eV), indicating partial graphitization. This result aligned with the earlier XRD findings of the formation of turbostratic carbon. The O 1s spectrum (Fig. 5c) revealed the contributions of Fe_3O_4 (530.57 eV), C=O/COOH (531.98 eV), and C–OH/COOH (533.28 eV), and confirmed the presence of oxygenated functional groups[64]. These findings were consistent with the FTIR spectra, which presented characteristic bands corresponding to these particular bonds. The Fe 2p spectrum (Fig. 5d) revealed the presence of metallic Fe^0 alongside Fe^{2+} and Fe^{3+}, which are characteristic of Fe_3O_4. The formation of mixed-valence iron oxides was confirmed by satellite peaks[65]. The coexistence of Fe^{2+} and Fe^{3+} in Fe_3O_4 implied that iron was oxidized during the high-temperature treatment and then reduced

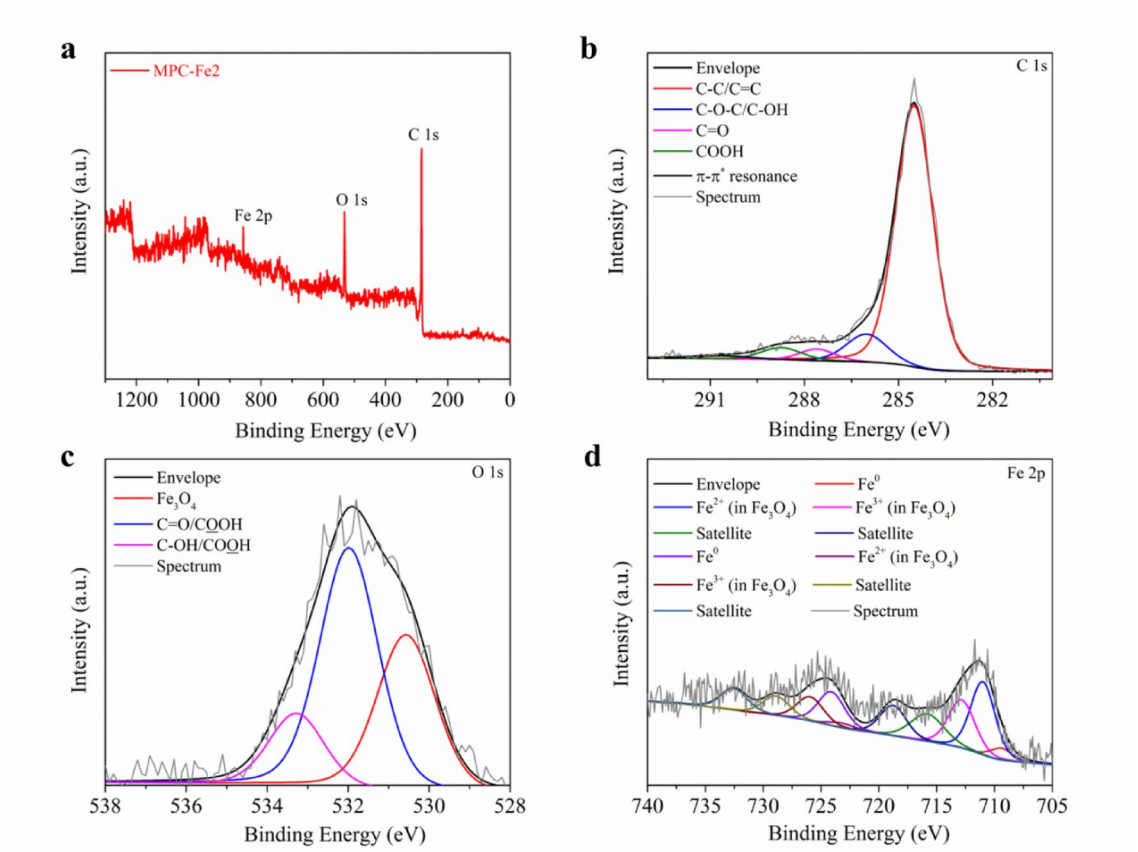

Fig. 5. (**a**) Wide scan of MPC-Fe2, and deconvolutions of high-resolution XPS spectra for elements in MPC-Fe2: (**b**) C 1s, (**c**) O 1s, and (**d**) Fe 2p.

to metallic Fe^0 in the carbon-rich environment. The XRD study also indicated the presence of both Fe^0 and Fe_3O_4 phases. Furthermore, the XPS analysis supported the SEM/EDS and TEM/EDS results, from which it was concluded that Fe_3O_4 and Fe^0 were present in addition to oxygen functionalities distributed across the carbon matrix. These findings highlighted the structural and chemical characteristics of MPC-Fe2 that could influence its physicochemical properties and potential applications.

Adsorption of tetracycline

To assess whether a given material will effectively remove a pollutant, it is necessary to understand the adsorption behavior of the pollutant on the adsorbent. The adsorption kinetics and isotherms of TC on MPC-Fe2 were investigated using different adsorption times and TC concentrations. Adsorption behavior was then determined from the non-linear fitting of the resulting data to kinetics and isotherm models.

The PFO and PSO kinetic models can be used to describe the adsorption kinetics of the magnetic carbon composite, comparing the two to establish which offers the better fit (Fig. 6a and b). The PFO model assumes that the adsorption rate is in direct proportion to the difference between the number of adsorbed molecules and the number of vacant sites. The relationship appears linear when concentrations are low, while saturation is reached as the concentration increases. The PSO model assumes that the adsorption rate is in proportion to the square of the number of available adsorption sites. This model typically works when the adsorption process is limited due to site availability rather than surface coverage. Given that the R^2 in this study was greater for the PSO model ($R^2 = 0.9991$), the PSO model more accurately represented the kinetics of adsorption of TC on MPC-Fe2. It was thus inferred that the rate-limiting step was connected to adsorption site availability rather than the adsorbate concentration gradient.

The adsorption isotherm for MPC-Fe2, along with the non-linear fitting obtained from the Langmuir, Freundlich, Temkin, and Guggenheim-Anderson-de Boer (GAB) models, are shown in Fig. 6c–f. These models were selected due to their common application in adsorption isotherm studies, with each providing different insights into the nature of the adsorption process. The Langmuir model, for instance, assumes monolayer adsorption on a surface with a finite number of identical sites, while the Freundlich model describes adsorption on heterogeneous surfaces with varying adsorption energies. The Temkin model accounts for the effects of indirect adsorbate-adsorbate interactions[66], and the GAB model is particularly useful for describing multilayer adsorption phenomena[67]. The fitting process was performed using a non-linear regression approach to minimize the sum of squared errors and obtain the best-fit parameters for each model. The corresponding parameter values and fitting results are presented in Table S3.

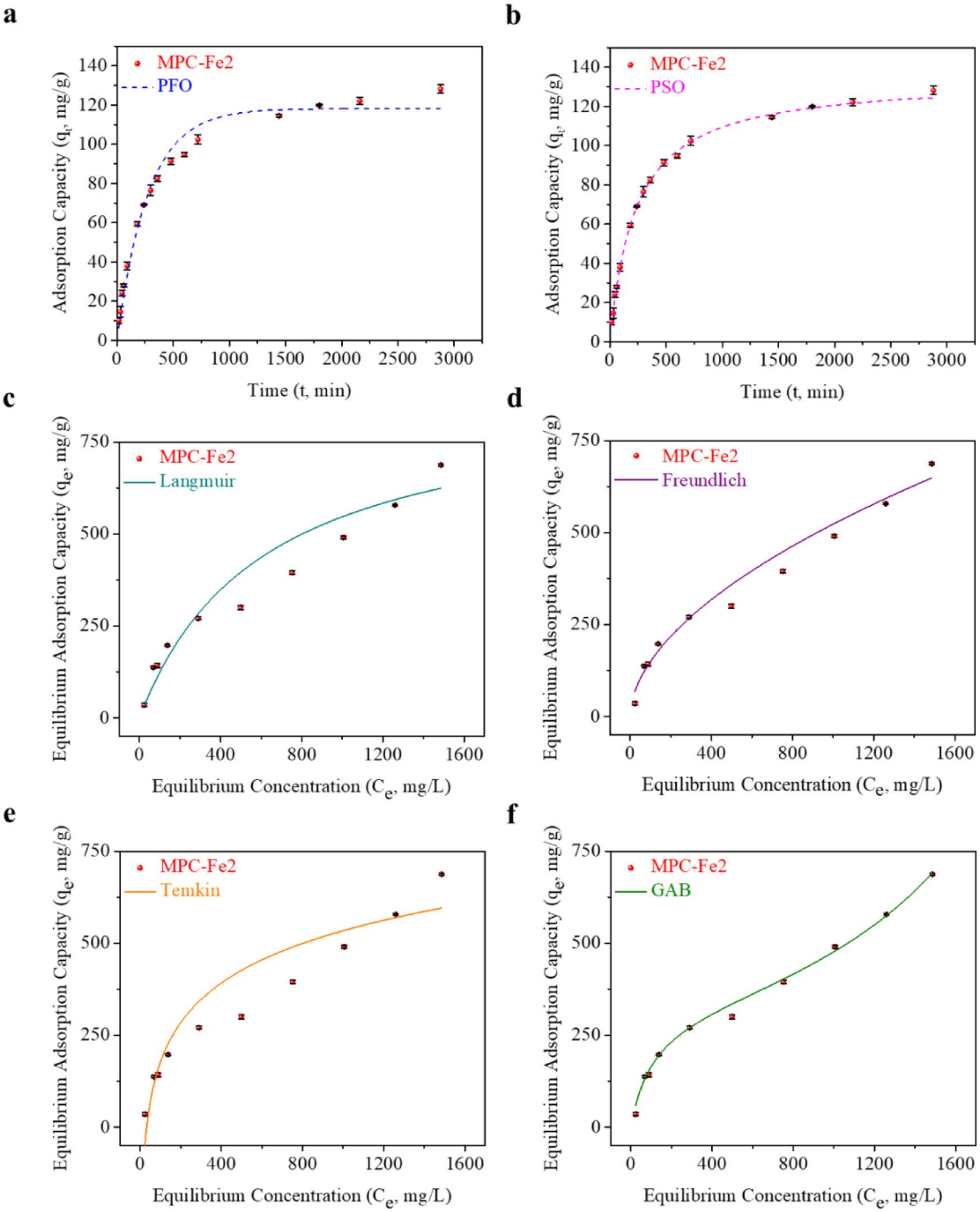

Fig. 6. Effect of contact time on tetracycline (TC) adsorption onto MPC-Fe2, with experimental data shown including standard deviation bars (in black), and non-linear fitting using: (**a**) pseudo-first-order (PFO) model, (**b**) pseudo-second-order (PSO) model. Adsorption isotherm data, also shown with standard deviation bars (in black), are fitted using non-linear models: (**c**) Langmuir, (**d**) Freundlich, (**e**) Temkin, and (**f**) Guggenheim-Anderson-de Boer (GAB).

Among the four isotherm models evaluated, the GAB model offered the best fit to the experimental data for tetracycline adsorption on MPC-Fe2, with a high coefficient of determination ($R^2 = 0.9971$). This model accounts for multilayer adsorption and incorporates intermolecular interactions beyond the initial monolayer. The fitted maximum monolayer adsorption capacity (q_m) was 319.4 mg/g, which is in good agreement with the observed adsorption plateau, indicating a reasonable representation of surface saturation. The model parameters, $K_1 = 9.45 \times 10^{-3}$ and $K_2 = 3.72 \times 10^{-4}$ L/mg, correspond to the affinity of tetracycline for the primary adsorption sites and the interaction strength contributing to multilayer formation, respectively. The highest adsorption capacity observed for MPC-Fe2 under the tested conditions was 687.6 mg/g, recorded at an initial tetracycline concentration of 1500 mg/L.

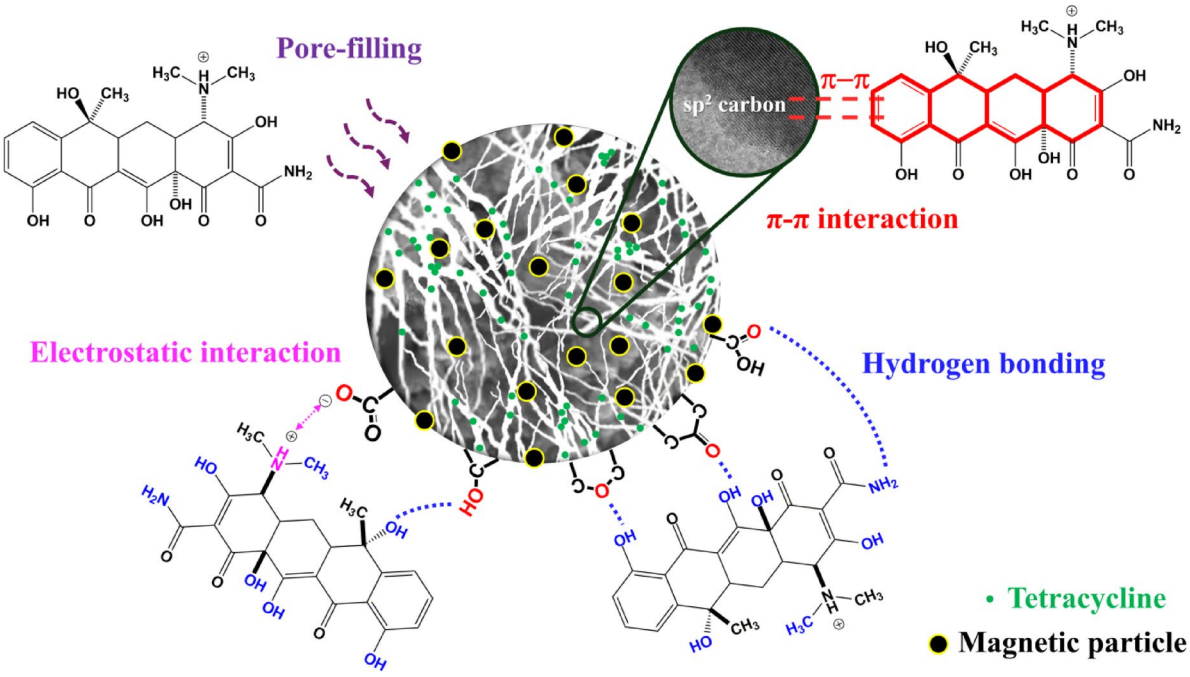

Fig. 7. Proposed adsorption mechanism of MPC-Fe2 for tetracycline.

Figure 7 illustrates the proposed mechanism of TC adsorption on MPC-Fe2. The process was influenced by the pore structure and surface chemistry of the adsorbent. According to both FTIR and XPS analyses, oxygen-containing functional groups were present at the carbon surface, including carbonyl (C=O), carboxyl (COOH), hydroxyl (C–OH), and ether (C–O–C). C=C bonds were also observed, which are typical of turbostratic structures. All of these functional groups were able to interact with TC molecules, generating adsorption sites that offered different levels of affinity, producing a heterogeneous adsorption process. In particular, π–π interactions between the aromatic rings of TC and the π-electron-rich turbostratic carbon formed strong bonds as the delocalized electrons overlapped[68]. Additionally, hydrogen bonding played a role in stabilizing adsorbed TC, as the $-NH_2$and –OH groups in TC could form hydrogen bonds with the oxygen-containing functional groups on MPC-Fe2[69]. Electrostatic interactions also contributed to the adsorption process, with the protonated secondary ammonium group in TC enhancing the interaction[70].

In addition to surface chemistry, adsorption was also affected by the pore structure of the adsorbent. The specific surface area of MPC-Fe2 was relatively large, at 505 m^2/g, while the total pore volume was 0.21 cm^3/g. The well-developed pore structure of the adsorbent enhanced the adsorption of TC. Since the surface area of the adsorbent was large, there were numerous sites where physical adsorption could occur, and the high pore volume helped accommodate TC molecules, which were readily confined within the pores[71]. Thus, the pores were efficiently filled, and the adsorbed species were stabilized. These synergistic effects resulted in a maximum adsorption capacity of 687.6 mg/g, highlighting the effectiveness of MPC-Fe2 in removing TC from aqueous solutions.

Adsorbent reusability

The reusability of an adsorbent is a critical property that lowers costs and allows large-scale systems to remain economically feasible. Adsorbent reusability was assessed here by running a series of adsorption-desorption cycles. In the initial cycle, the efficiency of pollutant removal was normalized to 100%, with subsequent cycles then compared to this base. Fig. S2a (left axis) shows that the percent removal was stable for the first three cycles but then slightly decreased to 95% by the fifth cycle, while the adsorbent retained its magnetic qualities as presented in Fig. S2b.

To ensure environmental safety and the potential for real-world applications, the iron leaching behavior of MPC-Fe2 was evaluated. Fig. S2a (right axis) presents the measured concentrations of iron released into solution after each cycle. The results confirm that the amount of iron leaching remained consistently low across all cycles, with concentrations well below the World Health Organization (WHO) guideline limit of 0.3 mg/L for iron in drinking water[72]. This finding is important, as excessive leaching of iron not only raises concerns about water quality and safety but also indicates structural degradation of the adsorbent. In this study, the minimal leaching observed suggests strong chemical stability of the iron species immobilized within the adsorbent matrix. Therefore, MPC-Fe2 not only demonstrates excellent reusability and magnetic separability but also meets safety standards for metal release, supporting its practical applicability in water treatment processes.

Comparative study

Table S4 provides a comparison of various iron-based magnetic carbon composite adsorbents for tetracycline removal, including the magnetic porous carbon composite (MPC-Fe2) prepared in this study. The key attributes highlighted include sources of magnetic properties, preparation methods, material properties, and adsorption performances. The MPC-Fe2 adsorbent stands out for its unique in situ protocol, which integrates carbonization, activation, and magnetization in a single step, making it more cost-effective, time-efficient, and energy-efficient than processes that separate these steps. Although other studies have sought to combine the three processes, they have mostly used external activators for pore creation, and commercial iron salts as the magnetic source, adding costs and complicating the process. The use of iron scrap for magnetization and pore activation along with the integration of the three steps is a much more sustainable approach. In terms of adsorption capacity, MPC-Fe2 ranks among the best reported so far, surpassing many other materials, possibly due to its large surface area, well-developed pore structure, and diverse surface functionalities. While it does not offer superior magnetization in comparison to some other adsorbents, its magnetic response is sufficient for easy and quick recovery of the adsorbent.

Conclusion

This study demonstrates the effective valorization of agricultural and industrial waste by using sugarcane bagasse and iron scrap to fabricate a highly efficient magnetic composite adsorbent that offers a sustainable approach to water purification. By integrating carbonization, magnetization, and activation in a single-step process, the synthesis not only reduces production costs but also saves time and energy compared to traditional multi-step methods. The use of iron scrap as both a magnetic precursor and a pore activator simplifies the synthesis process, eliminates the need for chemical activators, and supports the circular economy. The high adsorption capacity and reusability of the magnetic adsorbent material suggest its feasibility for large-scale water treatment. The easy recovery of the magnetic composite adsorbent further enhances its real-world potential. This work not only addresses the problem of water contamination but also offers a scalable, cost-effective, and environmentally friendly solution.

Data availability

The datasets generated and/or analysed during the current study are available in the Mendeley Data repository, DOI: https://doi.org/10.17632/pn3vdzng92.1.

Received: 1 April 2025; Accepted: 29 April 2025
Published online: 08 May 2025

References

1. Li, J. et al. Quality matters: pollution exacerbates water scarcity and sectoral output risks in China. *Water Res.* **224**, 119059 (2022).
2. He, Z., Cheng, X., Kyzas, G. Z. & Fu, J. Pharmaceuticals pollution of aquaculture and its management in China. *J. Mol. Liq.* **223**, 781–789 (2016).
3. Daghrir, R. & Drogui, P. Tetracycline antibiotics in the environment: a review. *Environ. Chem. Lett.* **11**, 209–227 (2013).
4. Xu, L. et al. Occurrence, fate, and risk assessment of typical Tetracycline antibiotics in the aquatic environment: A review. *Sci. Total Environ.* **753**, 141975 (2021).
5. Shi, Y. J. et al. Sorption and biodegradation of Tetracycline by nitrifying granules and the toxicity of Tetracycline on granules. *J. Hazard. Mater.* **191**, 103 (2011).
6. Jeong, J., Song, W. H., Cooper, W. J., Jung, J. & Greaves, J. Degradation of Tetracycline antibiotics: mechanisms and kinetic studies for advanced oxidation/reduction processes. *Chemosphere* **78**, 533–540 (2010).
7. Chen, A., Wang, N., Tian, Z., Wei, X. & Lei, C. One-step synthesis of readily recyclable Poplar sawdust-based porous carbon for the adsorption of Tetracycline. *Ind. Crops Prod.* **197**, 116621 (2023).
8. Ali, I. & Gupta, V. K. Advances in water treatment by adsorption technology. *Nat. Protoc.* **1**, 2661–2667 (2006).
9. Choi, K. J., Kim, S. G. & Kim, S. H. Removal of antibiotics by coagulation and granular activated carbon filtration. *J. Hazard. Mater.* **151**, 38–43 (2008).
10. Zhou, X. L., Zhang, H., Shao, L. M., Lü, F. & He, P. J. Preparation and application of hierarchical porous carbon materials from waste and biomass: A review. *Waste Biomass Valori.* **12**, 1699–1724 (2021).
11. Zafeer, M. K., Menezes, R. A., Venkatachalam, H. & Bhat, K. S. Sugarcane bagasse-based Biochar and its potential applications: a review. *Emergent Mater.* **7**, 133–161 (2024).
12. Nogueira, G. A. et al. Magnetic activated carbonaceous materials from sugarcane Bagasse: preparation, characterization, and hexavalent chromium removal. *Mater. Today Sustain.* **28**, 101040 (2024).
13. Rao Vaddi, D. & Malla, R. Geddapu, Satyanarayana. Magnetic activated carbon: A promising approach for the removal of methylene blue from wastewater. *Desalin. Water Treat.* **317**, 100146 (2024).
14. Zhang, S. et al. Porous magnetic carbon sheets from biomass as an adsorbent for the fast removal of organic pollutants from aqueous solution. *J. Mater. Chem. A.* **2**, 4391–4397 (2014).
15. Rattanachueskul, N., Saning, A., Kaowphong, S., Chumha, N., Chuenchom, L. & & Magnetic carbon composites with a hierarchical structure for adsorption of Tetracycline, prepared from sugarcane Bagasse *via* hydrothermal carbonization coupled with simple heat treatment process. *Bioresour Technol.* **226**, 164–172 (2017).
16. Liu, Y., Zhu, X., Qian, F., Zhang, S. & Chen, J. Magnetic activated carbon prepared from rice straw-derived hydrochar for triclosan removal. *RSC Adv.* **4**, 63620–63626 (2014).
17. Yimin, R., Abla, R., Dawut, G., Abdukayum, A. & Xiong, B. Preparation and adsorption performance of walnut Waste-Based magnetic activated carbon with high specific surface area. *ACS Omega.* **10**, 498–508 (2025).
18. Anyika, C., Asri, N. A. M., Majid, Z. A., Yahya, A. & Jaafar, J. Synthesis and characterization of magnetic activated carbon developed from palm kernel shells. *Nanotechnol Environ. Eng.* **2**, 16 (2017).
19. Li, C. et al. Performance and mechanism of a novel bamboo-based magnetic Biochar composite for efficient removal of Norfloxacin. *Adv. Compos. Hybrid. Mater.* **8**, 71 (2024).
20. Sun, M., Ma, Y., Yang, Y. & Zhu, X. Effect of iron impregnation ratio on the properties and adsorption of KOH activated Biochar for removal of Tetracycline and heavy metals. *Bioresour Technol.* **380**, 129081 (2023).

21. Rodríguez-Sánchez, S. et al. Sustainable thermochemical Single-Step process to obtain magnetic activated carbons from chestnut industrial wastes. *ACS Sustain. Chem. Eng.* **7**, 17293–17305 (2019).
22. Qin, Y. et al. Removal of Tetracycline onto KOH-activated Biochar derived from rape straw: affecting factors, mechanisms and reusability inspection. *Colloids Surf. Physicochem Eng. Asp*. **640**, 128466 (2022).
23. Mahawong, S. et al. Mesoporous magnetic carbon adsorbents prepared from sugarcane Bagasse and Fe^{2+} and Fe^{3+} *via* simultaneous magnetization and activation for Tetracycline adsorption. *Sci. Adv. Mater.* **12**, 161–172 (2020).
24. Thaveemas, P. et al. Magnetic carbon nanofiber composite adsorbent through green in-situ conversion of bacterial cellulose for highly efficient removal of bisphenol A. *Bioresour Technol.* **333**, 125184 (2021).
25. Thanh Do, T. V. et al. One-pot fabrication of magnetic Biochar by $FeCl_3$-activation of lotus seedpod and its catalytic activity towards degradation of orange G. *Mater. Res. Express.* **9**, 105601 (2022).
26. Cui, Y. et al. Biomass carbon magnetic adsorbent constructed by One-Step activation method for the removal of Hg^0 in flue gas. *ACS Omega*. **7**, 9244–9253 (2022).
27. Rattanachueskul, N. et al. Waste para-rubber wood Ash and iron scrap for the sustainable Preparation of magnetic Fenton catalyst for efficient degradation of Tetracycline. *Arab. J. Chem.* **17**, 105791 (2024).
28. Neslušan, M. et al. Microstructural transformation of a rail surface induced by severe thermoplastic deformation and its non-destructive monitoring via Barkhausen noise. *Wear* **402–403**, 38–48 (2018).
29. Ding, J. et al. Difference in the characteristics of the rust layers on carbon steel and their corrosion behavior in an acidic medium: limiting factors for cleaner pickling. *J. Clean. Prod.* **142**, 2166–2176 (2017).
30. Bhosale, M. A., Ummineni, D., Sasaki, T., Nishio-Hamane, D. & Bhanage, B. M. Magnetically separable γ-Fe_2O_3 nanoparticles: an efficient catalyst for acylation of alcohols, phenols, and amines using sonication energy under solvent free condition. *J. Mol. Catal. Chem.* **404–405**, 8–17 (2015).
31. Li, Y. et al. Controlled fabrication and characterization of α-FeOOH nanorods. *J. Inorg. Organomet. Polym. Mater.* **32**, 1400–1408 (2022).
32. Anderez, A., Alguacil, F. J. & López, F. A. Acid pickling of carbon steel. *Revista de Metalurgia* vol. 58 Preprint at (2022). https://doi.org/10.3989/revmetalm.226
33. Tang, B. et al. Minimizing the creation of spent pickling liquors in a pickling process with high-concentration hydrochloric acid solutions: mechanism and evaluation method. *J. Environ. Manage.* **98**, 147–154 (2012).
34. Cornell, R. M., Posner, A. M. & Quirk, J. P. Kinetics and mechanisms of the acid dissolution of goethite (α-FeOOH). *J. Inorg. Nucl. Chem.* **38**, 563–567 (1976).
35. Li, Q., Wang, A., Long, K., He, Z. & Cha, R. Modified Fenton oxidation of cellulose fibers for cellulose nanofibrils Preparation. *ACS Sustain. Chem. Eng.* **7**, 1129–1136 (2019).
36. Elarbaoui, S. Magnetite nanoparticles (Fe_3O_4 NPs) performed by the co-precipitation and green synthesis processes. *Main Group. Met. Chem.* **47**, 20230029 (2024).
37. Yu, N. et al. Surface S doping induced ladder-regulation of lattice oxygen on the vertical FeCoOOH for water oxidation. *Fuel* **376**, 132757 (2024).
38. Bedia, J., Peñas-Garzón, M., Gómez-Avilés, A., Rodriguez, J. J. & Belver, C. Review on activated carbons by chemical activation with $FeCl_3$. *C (Basel).* **6**, 21 (2020).
39. Xu, Z. et al. Understanding reactions and pore-forming mechanisms between waste cotton woven and $FeCl_3$ during the synthesis of magnetic activated carbon. *Chemosphere* **241**, 125120 (2020).
40. Lee, S. M., Lee, S. H. & Roh, J. S. Analysis of activation process of carbon black based on structural parameters obtained by XRD analysis. *Cryst. (Basel).* **11**, 153 (2021).
41. Joshi, P. et al. Adsorptive removal of multiple organic dyes from wastewater using regenerative microporous carbon: decisive role of surface-active sites, charge and size of dye molecules. *Chemosphere* **308**, 136433 (2022).
42. Hossain, M. D., Hossain, M. A. & Sikder, S. S. Hysteresis loop properties of rare Earth doped spinel ferrites: A review. *J. Magn. Magn. Mater.* **564**, 170095 (2022).
43. Onsri, P., Dubadi, R., Chuenchom, L., Dechtrirat, D. & Jaroniec, M. Highly porous carbons prepared *via* water-assisted mechanochemical treatment of cellulose-based materials followed by carbonization and mild activation. *Microporous Mesoporous Mater.* **364**, 112869 (2024).
44. Lu, F. et al. Study on full-scale pores characterization and heterogeneity of coal based on low-temperature nitrogen adsorption and low-field nuclear magnetic resonance experiments. *Sci. Rep.* **14**, 16910 (2024).
45. Bedia, J., Belver, C., Ponce, S., Rodriguez, J. & Rodriguez, J. J. Adsorption of antipyrine by activated carbons from $FeCl_3$-activation of Tara gum. *Chem. Eng. J.* **333**, 58–65 (2018).
46. Lv, Y., Zhang, Y. & Xu, Y. Understanding and technological approach of acid hydrolysis processing for lignocellulose biorefinery: panorama and perspectives. *Biomass Bioenergy*. **183**, 107133 (2024).
47. Isinkaralar, K. Improving the adsorption performance of non-polar benzene vapor by using lignin-based activated carbon. *Environ. Sci. Pollut Res.* **30**, 108706–108719 (2023).
48. Velusamy, K. et al. Role of Biochar as a greener catalyst in biofuel production: production, activation, and potential utilization – A review. *J. Taiwan. Inst. Chem. Eng.* **30**, 105732 (2024).
49. Han, M., Zhang, J., Chu, W., Zhou, G. & Chen, J. Surface-Modified sewage Sludge-Derived carbonaceous catalyst as a persulfate activator for phenol degradation. *Int. J. Environ. Res. Public. Health*. **17**, 3286 (2020).
50. Luo, Y. et al. Rice husk hydrochar prepared by hydrochloric acid assisted hydrothermal carbonization for Levofloxacin removal in bioretention columns. *Bioresour Technol.* **393**, 130105 (2024).
51. Barjasteh-Askari, F., Davoudi, M., Dolatabadi, M. & Ahmadzadeh, S. Iron-modified activated carbon derived from agro-waste for enhanced dye removal from aqueous solutions. *Heliyon* **7**, e07191 (2021).
52. Sert, S., Gultekin, Ş. S., Gültekin, B., Duran Kaya, D. & Körlü, A. A facile approach to produce activated carbon from waste textiles via Self-Purging microwave pyrolysis and $FeCl_3$ activation for electromagnetic shielding applications. *Polym. (Basel).* **16**, 915 (2024).
53. Balogun, A. O., Lasode, O. A., Li, H. & McDonald, A. G. Fourier transform infrared (FTIR) study and thermal decomposition kinetics of Sorghum bicolour glume and Albizia pedicellaris residues. *Waste Biomass Valorization.* **6**, 109–116 (2015).
54. Al-Gaashani, R., Najjar, A., Zakaria, Y., Mansour, S. & Atieh, M. A. XPS and structural studies of high quality graphene oxide and reduced graphene oxide prepared by different chemical oxidation methods. *Ceram. Int.* **45**, 14439–14448 (2019).
55. Onsri, P. et al. Dual-functional natural rubber latex foam composites for solar-driven clean water production and heavy metal decontamination. *Int. J. Biol. Macromol.* **273**, 133056 (2024).
56. Young, A. G., Green, D. P. & McQuillan, A. J. IR spectroscopic studies of adsorption of Dithiol-Containing ligands on cds nanocrystal films in aqueous solutions. *Langmuir* **23**, 12923–12931 (2007).
57. Khan, P. P. *et al. Chapter 10* - Evaluation of antimicrobial, antioxidant, and photocatalytic activity of zinc oxide nanoparticles synthesized from Parmotrema perlatum. in *Nanotechnology and In Silico Tools* (eds. Kaneria, M., Rakholiya, K. & Egbuna, C.) 141–154 (Elsevier, 2024). https://doi.org/10.1016/B978-0-443-15457-7.00019-8
58. Öner, F. O., Yürüm, A. & Yürüm, Y. Structural characterization of semicokes produced from the pyrolysis of petroleum pitches. *J. Anal. Appl. Pyrol.* **111**, 15–26 (2015).
59. Zou, C., Wu, Q., Gao, Z., Xu, Z. & Nie, F. The magnetic porous Biochar prepared by K_2FeO_4-promoted oxidative pyrolysis of Bagasse for adsorption of antibiotics in the aqueous solution. *Biomass Convers. Biorefin.* **14**, 14189–14205 (2024).

60. Thileep Kumar, K., Raghu, S. & Shanmugharaj, A. M. Transmogrifying waste blister packs into defect-engineered graphene-like turbostratic carbon: novel lithium-ion (Li-ion) battery anode with noteworthy electrochemical characteristics. *Nanoscale* **14**, 4312–4323 (2022).
61. Jin, S. et al. Ultrahigh strength and Modulus Graphene-Based hybrid carbons with AB-Stacked and turbostratic structures. *Adv. Funct. Mater.* **30**, 2005381 (2020).
62. Wang, D., Lian, J., Wang, Y., Jia, P. & Gao, F. Turbostratic lattice and electronegativity modification jointly enabled an Ultra-High-Rate and Long-Lived carbon anode for Potassium-Ion batteries. *ACS Appl. Mater. Interfaces*. **15**, 15585–15594 (2023).
63. Chen, X., Wang, X. & Fang, D. A review on C1s XPS-spectra for some kinds of carbon materials. *Fuller. Nanotub Carb N.* **28**, 1048–1058 (2020).
64. Pantea, D., Darmstadt, H., Kaliaguine, S., Sümmchen, L. & Roy, C. Electrical conductivity of thermal carbon Blacks: influence of surface chemistry. *Carbon N Y.* **39**, 1147–1158 (2001).
65. Wang, S., Hu, J. & Wang, J. Enhanced uranium removal from aqueous solution by core–shell Fe^0@Fe_3O_4: insight into the synergistic effect of Fe^0 and Fe_3O_4. *Chemosphere* **354**, 141730 (2024).
66. Ali, I., Hasan, S. Z., Garcia, H., Bentalib, A. & Imanova, G. Modeling of the adsorption of Tigecycline from water on $CoFe_2O_4$-Graphene nanocomposites. *Langmuir* **40**, 25599–25616 (2024).
67. Álvarez-Torrellas, S., Rodríguez, A., Ovejero, G. & García, J. Comparative adsorption performance of ibuprofen and Tetracycline from aqueous solution by carbonaceous materials. *Chem. Eng. J.* **283**, 936–947 (2016).
68. Gao, Y. et al. Adsorption and removal of Tetracycline antibiotics from aqueous solution by graphene oxide. *J. Colloid Interface Sci.* **368**, 540–546 (2012).
69. Zhang, X. et al. Standardization and micromechanistic study of Tetracycline adsorption by Biochar. *Biochar* **6**, 12 (2024).
70. Ngoc, D. M. et al. Tetracycline removal from water by adsorption on hydrochar and hydrochar-Derived activated carbon: performance, mechanism, and cost calculation. *Sustainability* **15**, 4412 (2023).
71. Wang, Z. et al. Insights into the adsorption behavior of Tetracycline in various shaped carbon nanopores: interplay between mass transfer and adsorption. *Microporous Mesoporous Mater.* **376**, 113197 (2024).
72. Zhou, Q. et al. Total concentrations and sources of heavy metal pollution in global river and lake water bodies from 1972 to 2017. *Glob Ecol. Conserv.* **22**, e00925 (2020).

Acknowledgements

This work was funded by the Basic Research Fund (BRF), Faculty of Science, Kasetsart University, and Prince of Songkla University (Grant No. SCI6801201S). S. Mahawong expresses appreciation to the Science Achievement Scholarship of Thailand (SAST) for supporting her studies. L. Chuenchom acknowledges the support from the Center of Excellence for Innovation in Chemistry (PERCH-CIC), Thailand. S. Kaowphong extends thanks to Chiang Mai University. N. Rattanachueskul also thanks the Graduate School, Prince of Songkla University, for PSU-PhD. scholarship (Contract No. PSU_PHD2562-003). Special recognition goes to Thomas Duncan Coyne, Faculty of Science, Prince of Songkla University, for his assistance with English proofreading and editing.

Author contributions

Sirinad Mahawong and Parichart Onsri contributed equally to investigation, validation, formal analysis, and writing – original draft. Piyatida Thaveemas participated in investigation, validation, and formal analysis. Sulawan Kaowphong, Supinya Nijpanich, and Natthanan Rattanachueskul were involved in investigations. Supanna Techasakul contributed to writing – review & editing, visualization, and supervision. Laemthong Chuenchom was responsible for conceptualization, methodology, formal analysis, writing – review & editing, project administration, and funding acquisition. Decha Dechtrirat contributed to conceptualization, methodology, validation, writing – original draft and review & editing, as well as funding acquisition.

Declarations

Competing interests

The authors declare no competing interests.

Additional information

Supplementary Information The online version contains supplementary material available at https://doi.org/10.1038/s41598-025-00610-5.

Correspondence and requests for materials should be addressed to L.C. or D.D.